

Mechanical Characterization Potentials of Aluminide Diffusion Coatings on Molybdenum Substrates

Jurica Filipovic,* Katharina Beck, Christian Kontermann, Mathias Galetz, and Matthias Oechsner

A mechanical test strategy is designed to determine the resistance of protective intermetallic aluminum layers on molybdenum substrates. Performing mechanical experiments, such as compression, four-point bending and indentation tests, the specific failure behavior and a potential impact of observed phase transformations within the interface zone on the structural integrity and adhesion strength are examined. Herein, the applied test structure aims at the description of damage characteristics and critical deformation states regarding the type of loading. In this respect, it focuses on delamination behavior under compressive load and crack channeling due to bending stress. The analysis of the mechanical experiments is supported by various measurement techniques, including 3D camera equipment (GOM) and an acoustic emission (AE) analysis system. In particular, the application of the AE technique in this work provides a helpful contribution to the detection of delamination failure and the development of multiple crack channeling. Considering the successfully applied experimental approaches, it is assumed that more complex coating-base material combinations can be characterized this way with respect to preceding annealing effects and the thereby influenced load capacity of thin films under different loading types.

high-temperature structures, which are usually based on Ni/Co or/and refractory metals, are provided with appropriate coatings protecting the structure-bearing material from the life-limiting influences of the environment. The research training group (RTG) *MatCom-ComMat* focuses on the development of such material systems consisting of polymer-derived ceramic nanocomposite^[1] and intermetallic protective coatings,^[2,3] as well as silicon-containing refractory metal-based substrate materials.^[4,5] Due to the challenging testability of the brittle metal silicides and the currently thin PDC top coats, aluminized molybdenum is investigated in this work with the main objective of developing suitable testing methods. A series of various mechanical tests after different annealing conditions is carried out at room temperature to develop a testing strategy to characterize the failure behavior and load-bearing capability of the material pairing. A further objective is to quantify a potential influence


1. Introduction

In the field of high-temperature applications, components might be exposed to extreme temperatures and aggressive media, which have a considerable influence on service life and load capacity. Depending on the application, materials of such

of phase transformations occurring within the layer structure on the adhesive strength of applied protective coatings. In this course, compression, four-point bending and indentation tests on aluminized molybdenum samples are performed to identify the load capacity and damage pattern as a function of loading type and to perceive applicable fracture mechanical models to describe the structural integrity of applied coatings and their application limits. The focus of the damage mechanisms is on delamination failure and the formation of multiple crack channeling, which could be recorded using various measurement techniques and the experimental tests mentioned. The use of in situ acoustic emission (AE) technology has proven to be particularly helpful in this context, which is why the results obtained are critically discussed in this study and classified with regard to their applicability for the analysis related to the observed failure characteristics.

J. Filipovic, C. Kontermann, M. Oechsner
Department and Institute of Materials Science (IfW)
Technical University of Darmstadt
Grafenstrasse 2, 64283 Darmstadt, Germany
E-mail: jurica.filipovic@tu-darmstadt.de

K. Beck, M. Galetz
Materials and Corrosion Division
DECHEMA Forschungsinstitut (DFI)
Theodor-Heuss-Allee 25, 60486 Frankfurt am Main, Germany

 The ORCID identification number(s) for the author(s) of this article can be found under <https://doi.org/10.1002/adem.202302027>.

© 2024 The Authors. Advanced Engineering Materials published by Wiley-VCH GmbH. This is an open access article under the terms of the Creative Commons Attribution-NonCommercial-NoDerivs License, which permits use and distribution in any medium, provided the original work is properly cited, the use is non-commercial and no modifications or adaptations are made.

DOI: 10.1002/adem.202302027

2. Experimental Section

The molybdenum base material was provided by *Plansee SE* with a purity of wt% > 99.97 in the form of a plate, from which cylindrical compression and cuboid bending specimens were manufactured at MPA-IfW (State Materials Testing Institute Darmstadt and Department and Institute of Materials Science, TU Darmstadt). The compression specimens had a height of

12 mm and a diameter of 9 mm, the cuboid bending specimens had dimensions of $50 \times 4 \times 3$ mm. Prior to coating, the specimens were ground at 180P and 500P before being cleaned in an ultrasonic bath with acetone. The subsequent coating process was performed by Dechema Forschungsinstitut in a tube furnace by pack cementation in an inert filler- and Al_2O_3 -containing powder basin with 1 wt% activator (NH_4Cl) and 1 wt% aluminum at 1050°C for 8 h.^[3] The resulting structural configuration of the material system is shown in the micrograph of **Figure 1**. The near-surface region is characterized by a two-phase intermetallic coating of thickness d_c consisting of an approximately $45\ \mu\text{m}$ Al_8Mo_3 and a $5\ \mu\text{m}$ AlMo_3 layer.

To develop a mechanical test strategy and potentially determine the resistance of the material composite regarding various loading aspects, a series of different mechanical tests series was conducted, including compression, four-point bending, and indentation tests. The same focus was on capturing observable damage mechanisms, which are assumed to be affected by pre-annealing, to create basic approaches for subsequent models. An overview of the tested samples, the test type and the corresponding annealing conditions is provided in **Table 1**. The pre-annealing temperature for exposure times of 100 h was varied in a range from 700 to 1300°C to induce a change in the coating architecture. Based on the damage mechanisms discussed in the section on mechanical results, the pre-annealing tests were carried out in an ambient atmosphere where possible (700 and 1300°C). For the temperature range from 800 to 1000°C , an inert environment had to be used due to the

susceptibility of the base material to oxidation, suspected pre-existing layer defects and the slower formation of a protective oxide layer. This circumstance, in addition to the shortened annealing time in the case of 1300°C , was taken into account and tolerated, as the general change in the coating characteristics after various annealing conditions was treated as a priority. Furthermore, it should be mentioned that the coating structure does not show any significant difference after pre-annealing at 1300°C for 50 h and 100 h, as a complete transformation of the coating into the AlMo_3 phase was observed at both annealing test conditions.

Both the compression and bending tests were accompanied by two main measurement techniques: a GOM 3D camera system for the optical resolution of the strain field and the visualization of the layer failure during the tests in addition to an AE analysis system for the acoustic detection of appearing events, which included cracking and the spalling of layer material. By means of these measurement methods, it was possible to analyze the damage process and draw conclusions about the critical deformations at which layer failure occurred. The selection and arrangement of the experiments were aimed not only at recording the layer failure and corresponding loading state but also at investigating the failure mechanisms. Delamination failure was the focus of the analysis in the compression tests, while the bending and indentation tests focused on the formation of segmentation cracks and multiple crack channeling. Both the recordings of the GOM system and the data of the AE system were directly linked to the recorded force and displacement values of the machines and the displacement transducers, allowing a specific assignment of recorded optical and acoustic data to defined load conditions. **Figure 2** shows the test setup for the compression and four-point bending tests. To resolve the optical strain field, a speckle pattern consisting of white developer as background and overlying graphite spray particles was applied to the samples prior to the experiments, as shown in **Figure 6a** as part of the results section of the compression tests.

While the AE sensors tracking the events during compression tests were attached to the compression stamps, in the case of bending tests, the piezoelectric sensors were attached directly to the specimen for a more sensitive detection of the low-energy signals in the course of the segmentation failure that occurs on the tensile-loaded side of the bending samples. In both cases, the sensor system was installed with plastic clamps and silicone paste to provide consistent contact pressure and assured signal flow in each test. Both types of tests were run in a strain- and deformation-controlled manner, respectively. The compression tests were run by means of two inductive *Solartron* displacement transducers with a compression speed of $0.025\ \text{s}^{-1}$, while the four-point bending tests were controlled to a displacement of $0.3\ \text{mm min}^{-1}$ via the displacement of the machine traverse. This specification resulted in a deflection of the equivalent of $0.075\ \text{mm min}^{-1}$, which was also recorded over the test runs using an inductive displacement transducer placed in the bottom center of the specimen.

2.1. Incremental Four-Point Bending

To obtain a more detailed overview of the load capacity and the failure behavior of the system with regard to segmentation crack

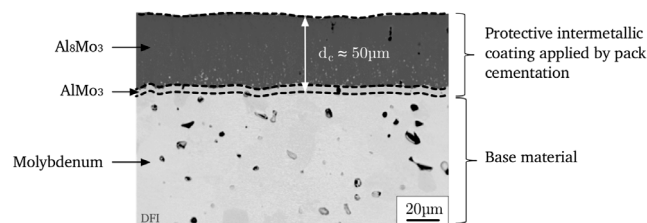


Figure 1. Micrograph of aluminized molybdenum in the initial state with the intermetallic protective coating containing Al_8Mo_3 and AlMo_3 phase.

Table 1. Overview of tested and analyzed samples, annealing conditions, and scope of use.

Sample ID	Temperature [°C]	Time [h]	Oxidation	Compression	Bending	Indentation
S3P4	1300	50	×	×	–	–
S3P14	–	–	–	×	–	–
S6P1/P10	–	–	–	×	–	–
S6P2	800	100	–	×	–	–
S6P3	900	100	–	×	–	–
S6P12	1000	100	–	×	–	–
S6B1/B5	–	–	–	–	×	–
S7B4	700	100	×	–	×	–
S7B5/B6	–	–	–	–	×	×
S7B10	–	–	–	–	×	–

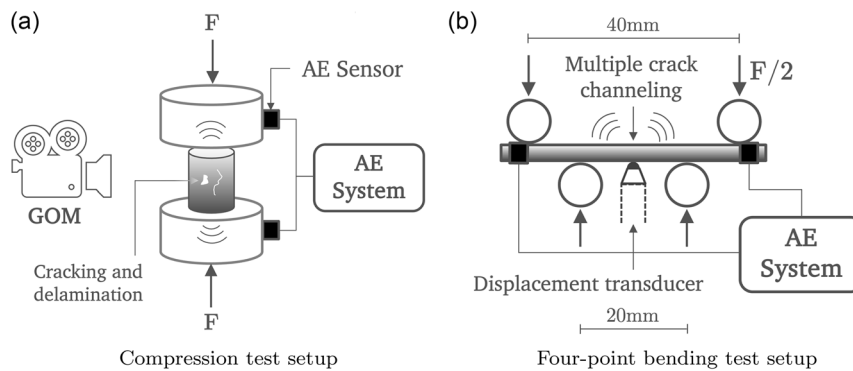


Figure 2. Setup of the experimental tests and overview of the measurement equipment including the GOM 3D camera and an AE system: a) compression test setup and b) four-point bending test setup.

development, the available specimens were partially subjected to an iterative bending test strategy. The aim hereby is to establish a nondestructive and rapid method for recording the crack channeling status after defined load conditions. This also reduced the number of samples and coating processes required for a primary characterization. An initially unloaded specimen was bent by a defined, incremental deflection s_{inc} in the center of the specimen. After reaching the defined deformation, the test was terminated, whereupon the relief curve and resulting permanent deflection of the specimen were captured.

Subsequently, the state of a fixed surface area (2×3 mm) on the tensile side was recorded using a digital microscope at $300\times$ magnification. As soon as the surface was recorded and the AE signals were analyzed for their characteristics, the sample was mounted again and repeatedly deformed by the previously determined deflection. Using this strategy, the segmentation crack network forming with regard to the loading condition was approximately analyzed nondestructively in the course of the test series, apart from the analysis via metallographic images. **Figure 3** outlines the procedure previously described.

2.2. Indentation Tests

To additionally characterize the integrity of the coating and the damage mechanisms occurring in the coating area, indentation tests were carried out on embedded bending specimens.

The main focus was placed on the segmentation cracks detected in the bending tests, which form with increasing stress. With the help of this additional test methodology, a more detailed description and a comparison to the results of the bending tests should be drawn. Incidentally, these specimens were already subjected to bending tests and reused for this type of test to maximize the utilization of existing test pieces. The methodology described in this paragraph is outlined in **Figure 4** and is based on approaches applied by Yamazaki,^[6,7] Marot,^[8] and Arai.^[9]

By means of Vickers indentation tests in the interface area between substrate and coating, (segmentation) cracks were induced both in the interface plane and perpendicular to the boundary. From preliminary tests, the focus was placed on the load levels HV0.1, HV0.2, and HV0.3, at which cracks were typically induced without regularly destroying the coating. The subsequent measurement of the cracks induced as a function of the load levels could contribute to the evaluation of the adhesive strength and crack resistance of the coating after evaluation and application of further methods. Since no coating delamination but only multiple crack channeling could be initiated during the bending tests, this method offers the opportunity for the approximation of an interface fracture toughness with regard to this material combination. Moreover, by recording induced segmentation cracks and comparing the stress to the load condition in the bending tests, a statement regarding the segmentation crack toughness could be made.

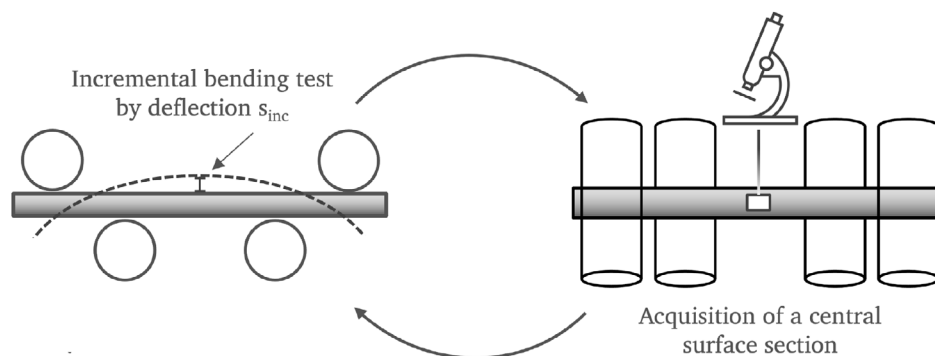


Figure 3. Overview of the incremental testing methodology within the framework of the four-point bending tests.

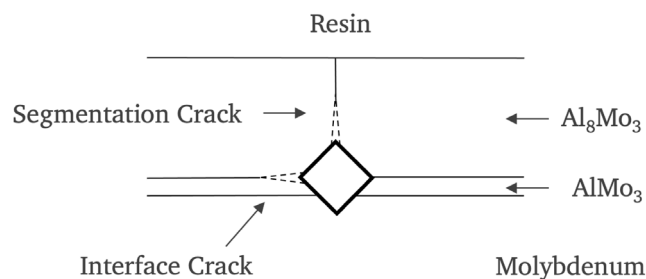


Figure 4. Systematics of indentation tests for the induction of segmentation and interface cracks.

3. Results

3.1. Annealing Experiments

The basis of the primary investigation of annealing effects on the failure characteristics of tested samples are annealing

experiments of aluminized molybdenum samples, both under atmospheric (700 and 1300 °C) and inert ambient conditions (800 to 1000 °C) (see Table 1). **Figure 5** shows microscopic images of the material system in its initial state and after different annealing conditions. From Figure 5a,b, it is evident that annealing at 700 °C after 100 h is not accompanied by discernible diffusion processes in the interfacial region and that the layer structure is comparable to the initial state of the sample. Only an oxide layer with a thickness of 100–200 nm, formed by the oxidation considered in this annealing configuration, distinguishes the system from the as-coated state. In comparison, annealing in the remaining temperature range from 800 to 1300 °C does result in noticeable transformations of the layer architecture, which are presented in Figure 5c–f. As can be seen in Figure 5c, heat treatment at 800 °C results in an increase of the aluminum-poor phase by 2–3 μm, while annealing at 1000 °C results in a tripling of the intermediate AlMo₃ phase (see Figure 5e).

Heat treatment at 1300 °C for 50 h is already reflected in a completely changed layer structure. The aluminum reservoir

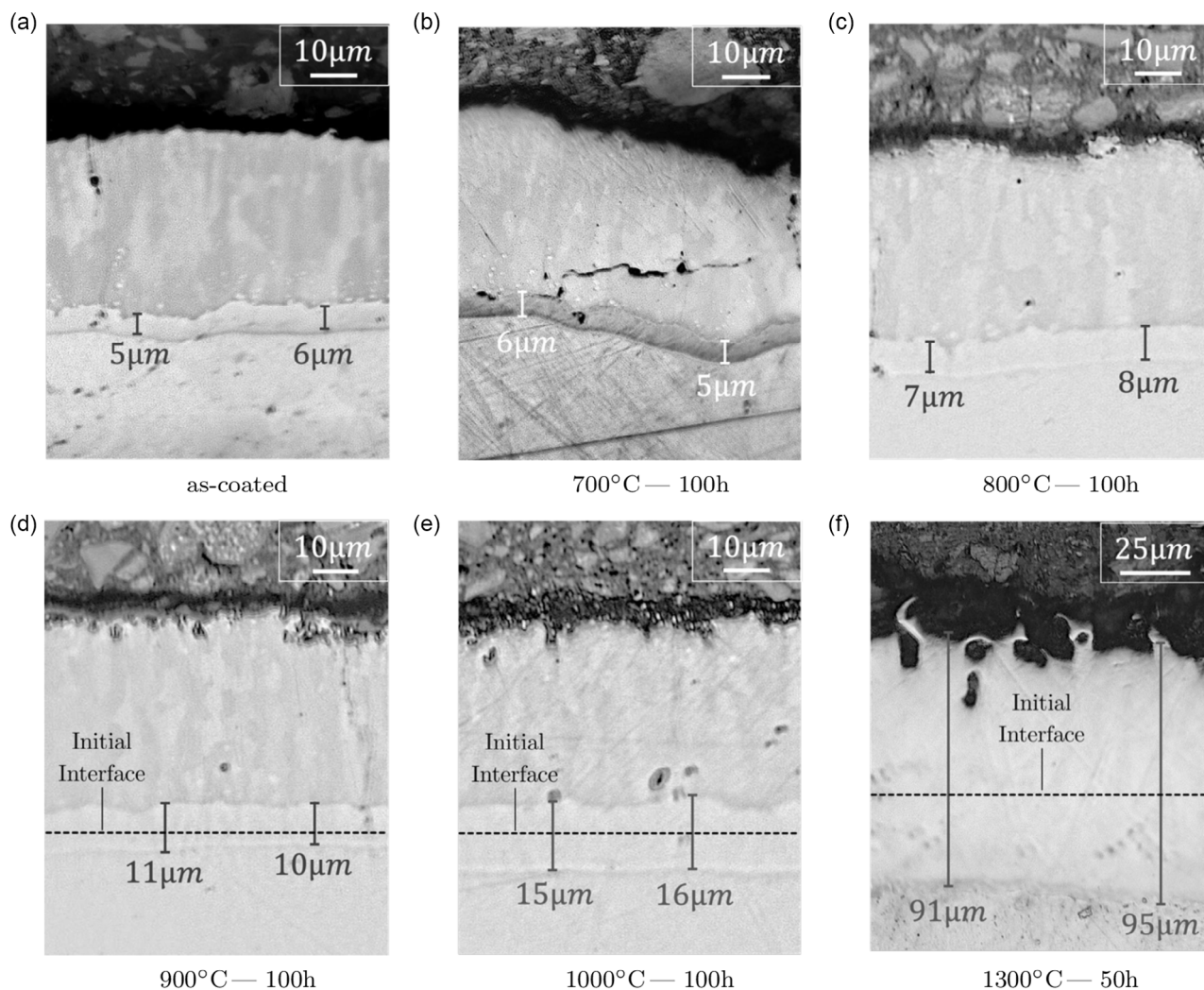


Figure 5. Micrographs highlighting the AlMo₃ phase range after different annealing temperatures and durations: a) as-coated, b) 700 °C—100 h, c) 800 °C—100 h, d) 900 °C—100 h, e) 1000 °C—100 h, and f) 1300 °C—50 h.

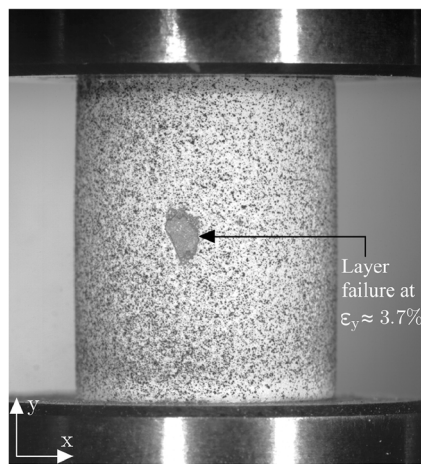
of the Al_8Mo_3 is consumed on the one hand by the oxidation taking place at the surface and on the other hand by the increased diffusion into the sample interior in this case. The oxide layer formed in the course of this annealing condition was dimensioned to a thickness of 7–8 μm . The changes in the layer structure relevant to the compression tests in this work for investigating the influence of preceding heat treatment on the critical deformation have therefore been specifically set and characterized via the growth of the brittle intermediate $AlMo_3$ phase.

3.2. Compression Tests

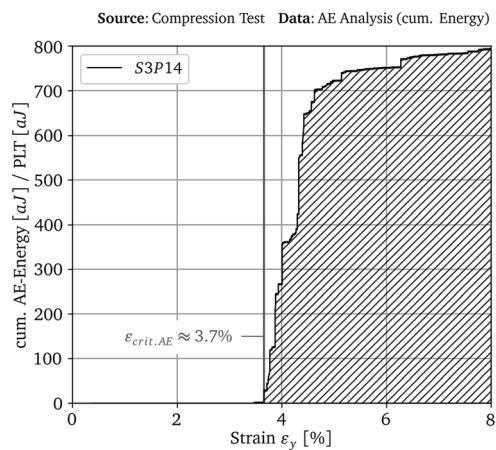
The compression tests carried out as part of this work are based on procedures performed by Adam et al.^[10] and aim at determining a critical compression of the material composite at which the load-bearing capacity of the material combination is exceeded. The associated layer failure basically manifests itself in sudden delamination failure. **Figure 6** shows the exemplary evaluation of compression sample S3P14 tested in as-coated state, whereby the

image recorded by the GOM at the time of failure is shown in **Figure 6a**. The associated critical compression of $\epsilon_y \approx 3.7\%$, at which first significant layer failure occurs, is determined via the displacement transducers. The reason for this is that the lack of speckle-patterned coating material in the evaluated area due to delamination presents a challenge when assessing the critical strain via the optical strain field. Looking at this example, the advantage of AE analysis can be identified, with the results of the same experiment being presented in **Figure 6b**. The cumulative energy of all acoustic events detected during the test is shown over the strain of the sample. According to the images of the 3D camera system, a drastic increase in the signal quantity and their respective energies can be observed at a critical strain of $\epsilon_{y,crit} \approx 3.7\%$.

The corresponding AE results are shown in **Figure 7**, which represents the normalized, cumulative energy of the detected signals over the strain of the respective test. The normalization of the data refers to the pencil lead test carried out immediately before the test and the average signal energy recorded. It should

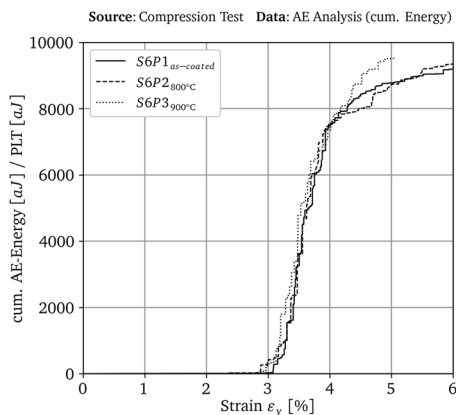


Optically detected and evaluated layer failure using GOM

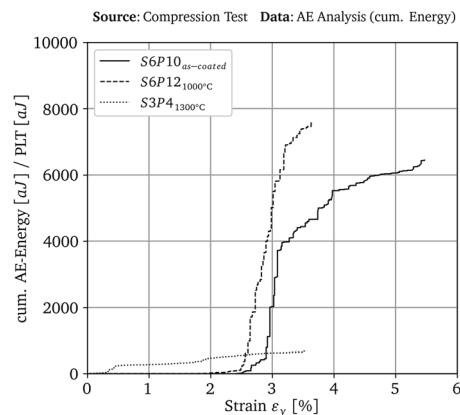


Cumulated AE energy indicating the layer failure at 3.7% strain

Figure 6. Layer failure of the compression specimen S3P14 (as-coated) at 3.7% strain detected by GOM and the AE system.



Cumulated energy for an as-coated specimen compared to an 800 °C and 900 °C (100 h) heat treated sample



Cumulated energy for an as-coated specimen compared to a 1000 °C (100 h) and 1300 °C (50 h) heat treated sample

Figure 7. Overview of the detected AE signals within the scope of the compression tests for the acquisition of critical compression and failure characteristics in dependence of pre-annealing.

be noted at this point that, for reasons of comparability, it was ensured that samples from the same coating batch were compared to avoid fluctuations in the coating result. Furthermore, annealing at 700 °C after 100 h was not taken into account, as no significant changes in the coating structure and phase distribution were observed, which could affect the susceptibility to coating failure. From Figure 7a, it can be assumed that annealing of the material compound at temperatures up to 900 °C for 100 h has no noticeable effect on the critical compression of the coated samples. In the case of both the as-coated and heat-treated samples, failure can be detected at a strain of 3%–3.1%. However, the comparison between as-coated and at/above 1000 °C heat-treated samples provides a different pattern (see Figure 7b). Although the cumulative AE signal energy of the as-coated sample S6P10 already increases at about 2.7% in this batch, the strongest increase and thus the failure to be interpreted as critical can be assigned to a compression of about 2.9%–3%, similar to before. The failure of the sample exposed to 1000 °C already increases steadily from about 2.5% strain, indicating a discreet difference in the critical strain due to pre-annealing. Based on the redistribution of the Al_8Mo_3 and AlMo_3 phase fractions on the coating presented in Figure 5e, the change in the load capacity can be associated with the pre-annealing of the corresponding sample. A repeatedly different failure behavior can be observed regarding the sample annealed at 1300 °C for 50 h. Both the very early detection of failure according to acoustic events after only 0.3% strain and the comparatively low energy clearly distinguish it from other performed tests. The classification of the sample annealed at this temperature is therefore not trivial and a direct comparison with the other tests is difficult, as both a different mechanical behavior and layer architecture due to heat treatment are present (see Figure 8).

In accordance with findings by Primig et al.^[11] the reason for the changed mechanical behavior, which is highlighted in Figure 8a, are recrystallization processes in the base material, which occur increasingly at temperatures above 1100 °C and cause noticeable softening. Despite this fact, the experiment provides an insight into the assignment of the acoustic signal energies to the respective damage patterns of the examined samples (see Figure 8b). The evaluations of the microscopic sections from Figure 5 show that the layer area of the as-coated/1000 °C sample

differs fundamentally from the one heat-treated at 1300 °C and that the latter is only composed of the AlMo_3 phase.

While the failure of the two-phase coating manifests itself in a large-scale delamination of the Al_8Mo_3 phase along the surface, in the case of the sample annealed at 1300 °C only isolated, comparatively small-scale chipping of the coating can be observed in addition to the flaking of the relatively thin oxide layer. The majority of the AlMo_3 phase, which is noticeably more pronounced in this case, is still intact, similar to the samples compared. The different results with regard to the damage pattern and the underlying failure mechanisms arrange themselves according to the level of cumulative acoustic energies detected and reflect the discrepancy observed.

3.3. Four-Point Bending Tests

The initial aim of the four-point bending tests was to induce a potential delamination failure of the coating as a result of the bending stress and derive values for fracture toughness based on crack initiation in the interface. This could not be realized even after various modifications of the coating and specimen properties, whereas so-called multiple crack channeling, which is described in detail by Hutchinson and Suo,^[12] was observed on the side of the bending specimen subjected to tensile stress in every case. From the experience gained in the course of the compression test series, the focus has been set on the optical and AE-assisted recording and characterization of progressive coating segmentation due to bending impact. The bending test series primarily focuses on the design and critical examination of the incremental bending test procedure. Using the sample S7B10, a preceding series of bending iterations was carried out with subsequent optical analysis of the surface condition. The relevant results with regard to bending stress and deflection, as well as the optical characterization and evaluation of the resulting segmentation crack pattern, are shown in Figure 9 and 10.

To first determine the influence of the iterative approach on the load condition of the specimen with regard to defined deformation states, the stress–deflection data of the incrementally tested specimen is compared to that of a conventionally bent specimen (see Figure 9a). From this, a slightly increasing

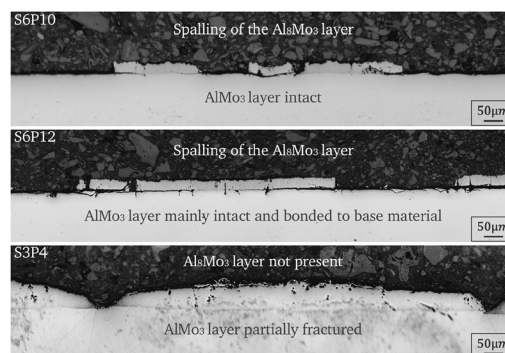
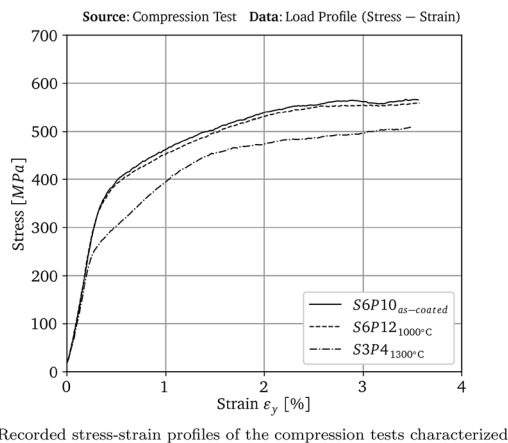
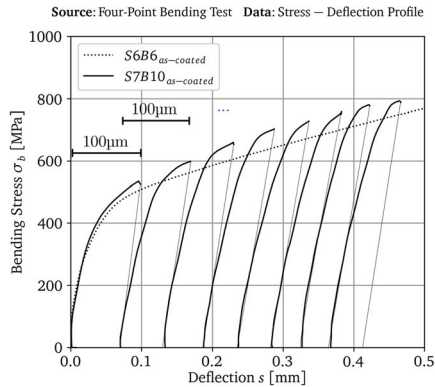
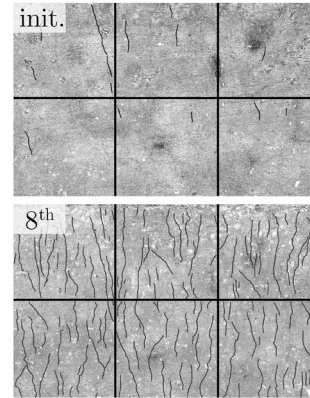


Figure 8. Stress profiles and microscopic images of the pressure samples in the as-coated state and after annealing at 1000 °C/1300 °C.



Load profiles of incremental tests with a deflection of $s_{inc} = 100 \mu\text{m}$ (S7B10) compared to a continuous bending test (S6B6)

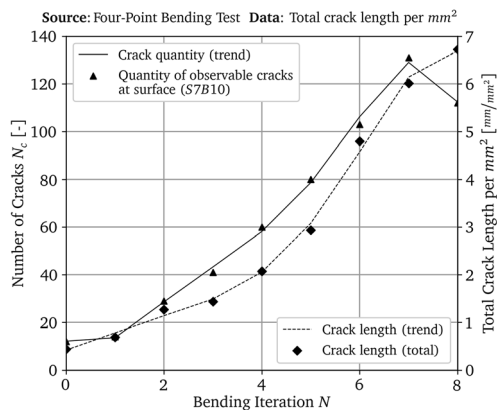


Surface images at initial state and after the 8th bending test run

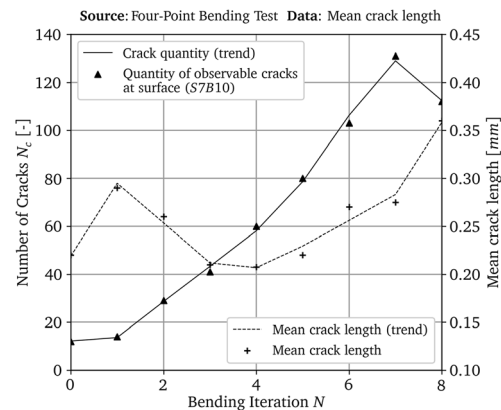
Figure 9. Iterative load profiles and sections of surface images of the S7B10 bending specimen with annotated segmentation cracks.

deviation of 20–50 MPa can be observed, especially from the second test run onward. This observation is certainly connected to minor differences in sample and coating properties along with the major effect of cycle-load-induced hardening of the test specimen considered. This deviation was accepted for the first optical comparison of the respective surface conditions. The corresponding images of the investigated section on the tensile side of the specimen in the initial state and after the eighth bending iteration can be seen in Figure 9b. From this analysis and primarily manual annotation of visible cracks in the surface plane, it is obvious that the applied bending loadings of the first eight test runs result in a clearly recognizable formation of multiple crack channeling. In view of the selected resolution, the difficulty in recording the curved surface without errors and the fact that not all cracks are equally wide open, it is currently not possible to detect all existing cracks in this way. Nevertheless, the analyzed images were taken into account for a rough estimate of the segmentation crack development. Starting from the reference state to the end of the iteration series, all images of the analyzed section were examined with regard to their crack characteristics.

The corresponding findings are shown in Figure 10 and focus on the number of visible cracks, the total crack length per mm^2 , and the mean crack length. This evaluation indicates that the number of cracks recorded rises steadily with each bending test and increases approximately tenfold in the course of the experiments carried out. After the last deflection, a decrease in the total number of cracks was observed, which is largely related to the merging of individual cracks in the induced deformation state. While the total crack length per unit area recorded in accordance with the increasing number of cracks rises as expected with each iteration, the average crack length should be viewed with caution. The influence of the surface condition in the initial state can be clearly seen here, as even at the beginning, a few isolated but comparatively long cracks could be observed. As the number of cracks increases, there is an almost constant increase in the average crack length from the fourth iteration onward. Despite the fact that a purely visual and complete detection of all segmentation cracks currently proves to be difficult overall, the characterized crack channel states have been used for the planning of subsequent bending tests and targeted deformation states.



Overview of the total crack length per mm^2 and the number of cracks over the individual bending iterations



Plot of the mean crack length and the number of cracks over the isolated bending iterations

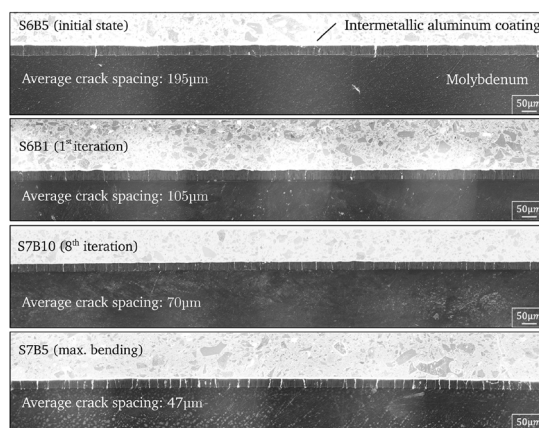
Figure 10. Characteristics of the segmentation crack network of sample S7B10 evaluated via nondestructive optical analysis of a defined surface section.

An indicator of this are the findings presented in the following section, which were obtained from micrographs and AE measurement data. The crack opening in the respective states significantly impairs successful optical crack detection. While the actual mean crack spacing can be detected in places after eight iterations by this method, this is not yet realistic in the initial state or after the first break-off tests. As previously indicated, microscopic images and the findings obtained using AE provide a more accurate picture of the crack density during the formation of the segmentation crack pattern. **Figure 11a** shows ≈ 1.8 mm wide, representative microsections of the surface-near material state of samples in the initial state, after different numbers of break-off tests (1st and 8th bending increment) and after a critical single bending to a deflection of 1.25 mm. The range evaluated to determine the mean crack distance of all specimens is ± 6 mm starting from the center of the bending specimen. The deflection designated as critical refers to a deformation and stress state in which, on average, a catastrophic failure occurs in the form of a large-area layer spalling on the compression side in the region of the inner supports. The number of cracks and the measured crack distances provide the values of the average crack spacing plotted in **Figure 11b** with regard to the resulting and permanent deflection in the center of the specimen after the tests.

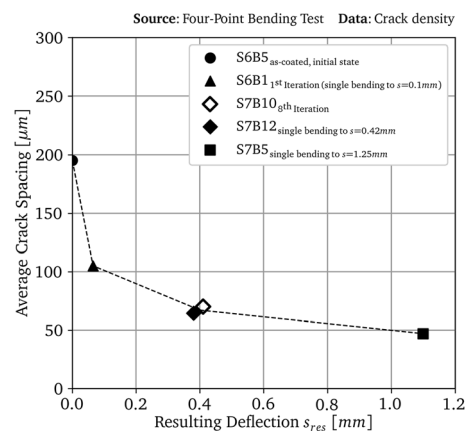
The result of this once again optically based investigation suggests that the onset of layer segmentation in terms of multiple crack channeling already occurs during the first bending iteration. This is supported by the approximate reduction by 50% of the mean crack spacing in the initial state (S6B5) from about 195 to 105 μm after the first bending test (S6B1). In the further course of the deflection based on the iterative bending steps and individual single bending tests, the value of the average crack spacing decreases steadily and approaches the layer thickness $d_c \approx 50$ μm , as indicated by the evaluation of sample (S7B5). This mean crack distance could also be recorded for a sample that was completely bent in a single pass, with a resulting deflection of 1.8 mm. These findings point to this being the maximum provokable segmentation crack density of this material composite in the bending stress range investigated.

The development of the layer segmentation observed with this analysis is also reflected in the recorded data of the AE system with regard to the eightfold iteratively bent sample S7B10 (see **Figure 12**). In the diagram of **Figure 12a**, the amplitudes of all occurring acoustic signals of the eight break-off tests are plotted on top of each other and as a function of the respective deflection of 0–100 μm . The stacked data sets are limited to the maximum recorded amplitude interval of 50–80 dB in each case. On the basis of this data set, both the number of events detected in the first bending test and their mean amplitude significantly exceed those of the subsequent bending iterations. The level of maximum signal density and strength is already reached from a deflection of about 10 μm , signaling a very eventful damage behavior within the range of the attached AE sensors. From the second bending iteration onward, there is a noticeable and steady decrease in the detected signals as well as the average amplitude over the test series. This observation could be related to the lower increase in the crack density presented in **Figure 11b**.

To ensure that the detected events are actually signals from the test zone of the bending specimen between the inner supports, the local origins of the events are considered in **Figure 12b**. Using the example of the first bending iteration, the absolute energies of the signals are plotted over the deflection and the location along the sample (± 25 mm). At first, the detection of the initial high-energy signals and the presumably associated layer damage can be repeatedly assigned to a deflection of about 10 μm . Additionally, it can be seen that approximately 84% of the total 3400 recorded signals originate from the test zone of -10 to 10 mm between the inner supports characterized by a constant bending moment. Also, most of the detected high-energy signals (>10 f) are equally concentrated in this area. To examine further that the detected signals in fact originate from the tensile side of the bending sample and that any potential damage to the remaining coated sample surfaces is neglected by the acoustic measurement system as far as possible, the piezoelectric sensors were attached directly to the tensile-loaded surface^[13] during the bending test of sample S6B1 and weighted down.

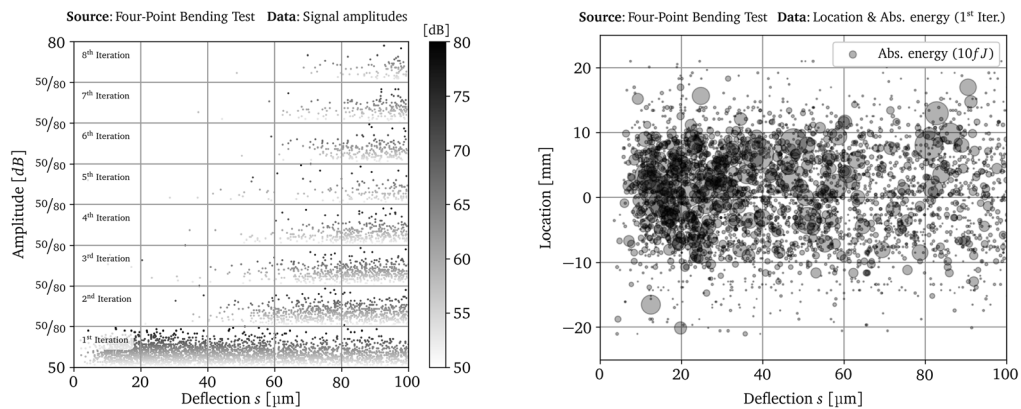


Micrographs of four-point bending samples highlighting the average crack spacing depending on the deflection state



Development of the mean crack spacing as a function of the resulting deformation state after bending

Figure 11. Analysis of the average segmentation crack spacing by means of microscopic images after different bending iterations and as a function of the residual deformation state.



Visualization of the events and signal amplitudes during the individual bending iterations over the respective deflection of 100 μm

Overview of the acquired signals and their absolute energy over the specimen length and the deflection during the first bending iteration

Figure 12. Detected signals of AE for sample S7B10 from the first to the eighth iteration.

The results of this experiment are shown in **Figure 13** and present a very similar outcome to the data in **Figure 12b**. In both cases, a comparable failure pattern can be observed, which also supports the observation of layer segmentation already beginning in the course of the first iteration, mainly located in the evaluated test zone. An initial estimate of the applied stress, which results in the initiation of segmentation cracks starting from the initial state, can be made roughly by considering the stress profiles of the sample S7B10 from **Figure 9a**. At a deflection of 10 μm , a maximum of about 200 MPa is acting at the outer surface, with the entire sample still being loaded elastically. According to the data shown, it can be assumed that this very stress level at the beginning of the iteration series results in the nucleation of a further set of cracks within the layer segments on the tensile side of the sample. Nonetheless, the respective characteristics of the crack network, i.e., the prevailing crack density at the beginning of a bending test, combined with the influence of potentially introduced residual stresses during iterative

bending tests, must be taken into account. The work of Hutchinson,^[12] Thouless,^[14] and Delannay^[15] provides fundamental approaches and principles for the consideration of the outlined challenge and the characterization of the observed failure behavior.

To further investigate the aforementioned thesis, the diagrams of **Figure 14** show the development of the AE signal accumulation together with the resulting crack density over deflection of the respective tests. The data presented shows that the characteristic course of the segmentation development, with the average crack spacing approaching the layer thickness, is reflected in the decrease in the detected acoustic signals. While increased acoustic activity with an accompanying significant decrease in the mean crack spacing can be identified at the beginning of the bending tests, both the segmentation crack density and the accumulation of detected AE signals approach a plateau from higher deflections with a similar deformation state. This result was observed in all bending tests performed, suggesting the applicability and spectrum for acoustically based analysis of the damage mechanism considered in different load situations and for varying layer structures.

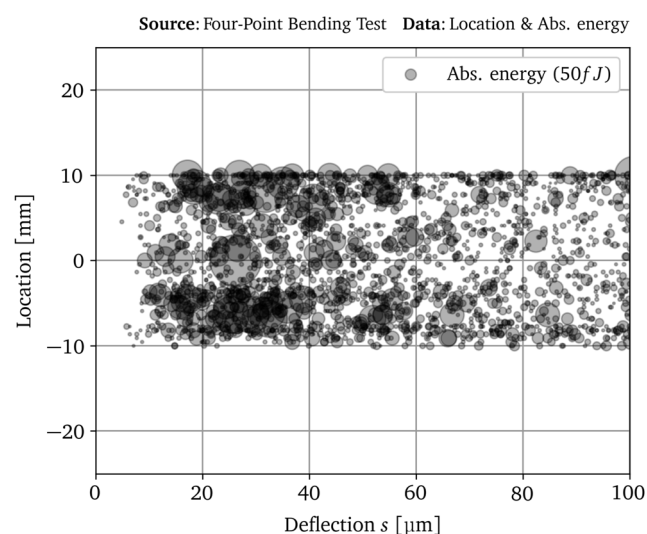


Figure 13. Detected signals by AE analysis for sample S6B1 during the first bending iteration.

3.4. Indentation Tests

To gain additional insight into the crack initiation susceptibility and crack growth behavior in the area of the coating, Vickers hardness indentations were performed at the interface to primarily induce interfacial cracks between the phases of the coating. The main reason for this placement is related to the findings of the compression tests, which have shown that delamination and spalling as catastrophic failure mechanisms are mainly limited to the Al_8Mo_3 phase along the surface. Since the exact positioning of the indenter tip at the interface proved to be quite difficult, 10 indentations were performed for each load level. The representative images and corresponding evaluation with respect to the induced cracks for the different load levels can be found in **Figure 15** and **Table 2**. Overall, it was possible to induce segmentation cracks perpendicular to the interface in almost all cases. Note that a load interval could be identified

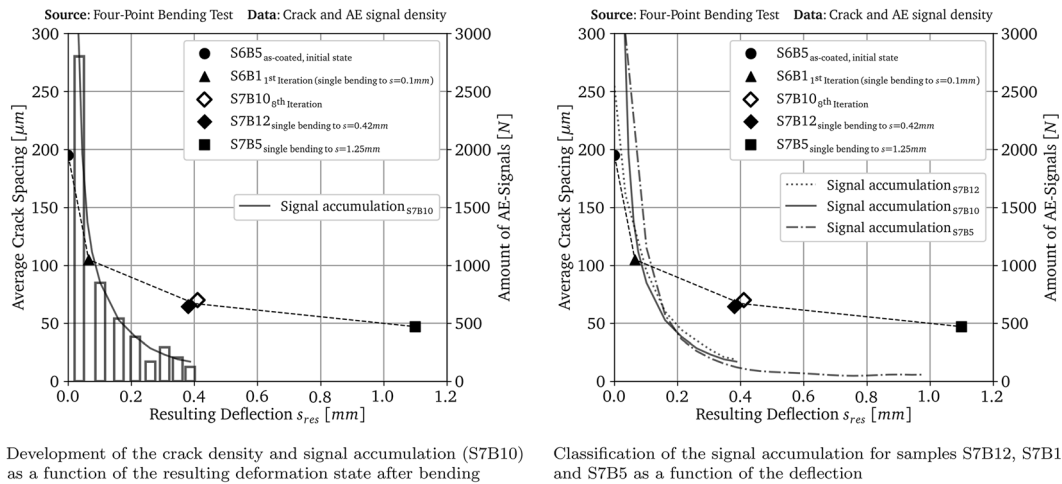


Figure 14. Analysis of the average segmentation crack spacing and AE signal accumulation as a function of the residual deformation state.

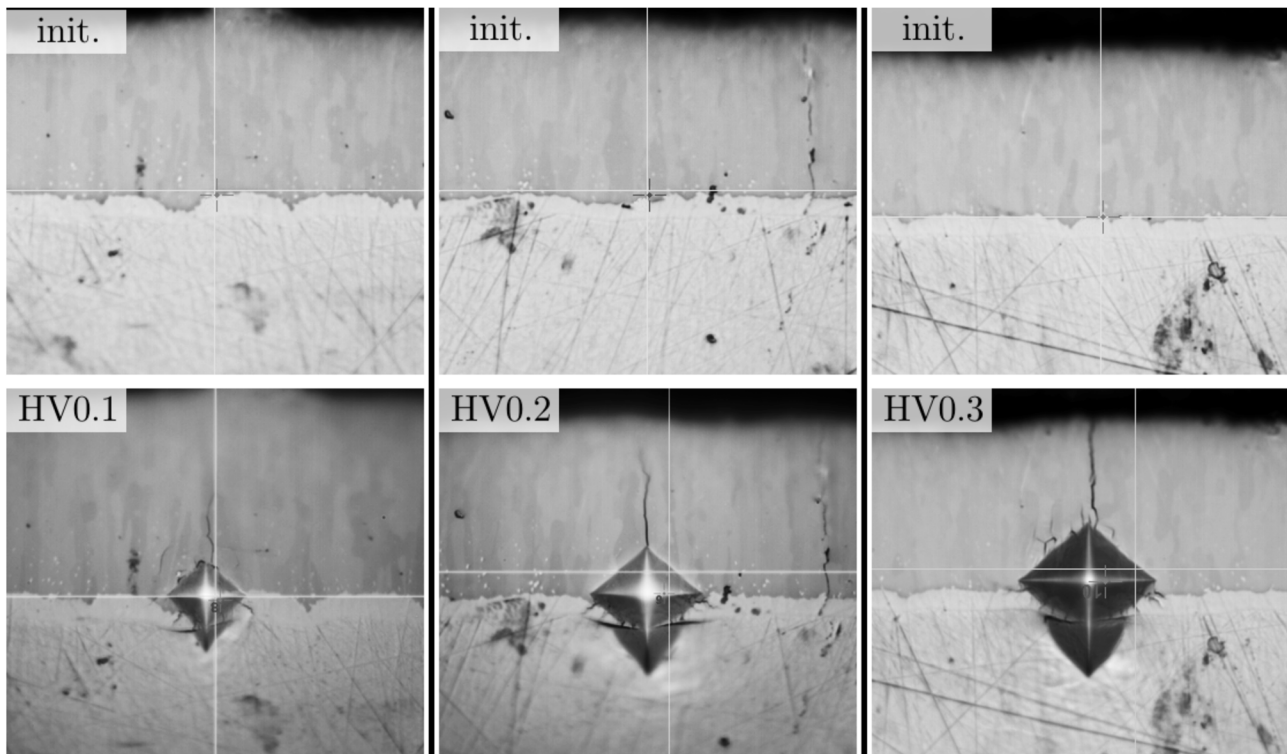


Figure 15. Exemplary images of the hardness indentations under load levels HV0.1, HV0.2, and HV0.3 at the interface of the investigated material composite.

in which the average length of the induced cracks can be brought into line with the selected indentation load. While the mean length of cracks initiated vertical to the interface at the lowest load is about $14.5\ \mu\text{m}$, it shows larger values of $20.5\ \mu\text{m}$ (HV0.2) and $24.5\ \mu\text{m}$ (HV0.3) at the higher load levels. Nevertheless, testing at HV0.3 proved to be critical, as there is an increased tendency toward complete tearing of the coating, which complicates the interpretation of the experiments. The reason for this is that the assignment of a resulting mean crack length to a defined load by the indentation is not clear.

In contrast, the initiation of interfacial cracks between the phases of the coating was associated with difficulties. Both the positioning of the indentation and the evaluation of the successfully induced interfacial cracks play a role here, as these do not propagate uniformly along the $\text{Al}_8\text{Mo}_3\text{-AlMo}_3$ interfaces but kink within the AlMo_3 phase. In addition, the extent of the interface cracks cannot currently be correlated with the selected load level, as can be seen from the relatively small average crack length at the highest load (HV 0.3) compared to the other indentation loads. Additional background on the classification of the

Table 2. Number and average length of induced interface and segmentation cracks after performing 10 hardness tests per load level.

Load level	Segmentation cracks	Mean crack length [μm]	Interface cracks	Mean crack length [μm]
HV0.1	9	14.5	11	4.5
HV0.2	10	20.5	14	5.6
HV0.3	9	24.5	11	2.9

results under the test conditions mentioned is provided by findings from Yamazaki.^[7] Essentially, it should be noted that despite the challenging induction of interface cracks, a method for the gradual and defined generation of segmentation cracks was identified in the material system investigated, which can be systematically related to the damage pattern of multiple crack channeling observed in the bending tests.

4. Conclusion

As part of the investigation of aluminized molybdenum, it was possible to elaborate approaches for characterizing discovered failure patterns depending on different types of loading. Using the 3D camera equipment (GOM) and in particular the AE analysis system, first failure-critical loading states of coated samples, such as critical strains in the compression tests along with damaging deflections and failure characteristics in the bending experiments, were identified. For instance, the evaluation of the compression tests provided results indicating that not only the critical load at the time of coating spalling can be determined, but also a different, lower-energy failure mechanism due to a changed coating structure could be observed. In the course of iterative bending tests, the occurrence of multiple crack channeling was recorded and the abrupt formation of new sets of cracks in existing layer segments locally and as a function of the deflection was detected successfully. To establish the nondestructive study of segmentation crack formation in subsequent bending tests, a higher resolution of the images and a computer-aided analysis of the optical images using classical (thresholding, noise filters) techniques are being considered. In combination with the latest results of indentation tests, in which different crack characteristics were witnessed depending on the applied load level, the description of crack growth using fracture mechanical methods and the use of structural mechanics calculations can be examined in more detail. In the selected load range, the applied procedure offers the possibility to set defined segmentation crack states and to examine the failure pattern of multiple crack channeling with regard to the growth of individual cracks and associated fracture mechanical studies.

Acknowledgements

The authors would like to thank their colleagues from DFI for carrying out the coating process and for all inspiring and helpful discussions. This work

was carried out within the framework of the German Research Foundation (DFG)-funded *MatCom-ComMat* research training group. The authors are therefore grateful to the DFG for its financial support of the RTG, whose members are also thanked for their support and discussions. Further appreciation is directed to *Plansee SE* for providing the molybdenum base material.

Open Access funding enabled and organized by Projekt DEAL.

Conflict of Interest

The authors declare no conflict of interest.

Data Availability Statement

The data that support the findings of this study are available from the corresponding author upon reasonable request.

Keywords

acoustic emission, crack channeling, intermetallic coating, thin-film characterization

Received: November 29, 2023

Revised: February 5, 2024

Published online: May 3, 2024

- [1] J. Yuan, M. Galetz, X. Luan, C. Fasel, R. Riedel, E. Ionescu, *J. Eur. Ceram. Soc.* **2016**, *36*, 3021.
- [2] K. Beck, F. Hinrichs, C. Oskay, A. S. Ulrich, M. Heilmaier, M. C. Galetz, *Coatings* **2023**, *13*, 10.
- [3] K. Beck, A. S. Ulrich, A. K. Czerny, E. M. White, M. Heilmaier, M. C. Galetz, *Surf. Coat. Technol.* **2024**, *476*, 130205.
- [4] D. Schliephake, A. Kauffmann, X. Cong, C. Gombola, M. Azim, B. Gorr, H.-J. Christ, M. Heilmaier, *Intermetallics* **2019**, *104*, 133.
- [5] F. Hinrichs, A. Kauffmann, A. S. Tirunilai, D. Schliephake, B. Beichert, G. Winkens, K. Beck, A. S. Ulrich, M. C. Galetz, Z. Long, H. Thota, Y. Eggeler, A. Pundt, M. Heilmaier, *Corros. Sci.* **2022**, *207*, 110566.
- [6] Y. Yamazaki, S.-I. Kuga, T. Yoshida, *Acta Metall. Sin. Engl. Lett.* **2011**, *24*, 109.
- [7] Y. Yamazaki, M. Arai, Y. Miyashita, H. Waki, M. Suzuki, *J. Therm. Spray Technol.* **2013**, *22*, 1358.
- [8] G. Marot, P. Démarécaux, J. Lesage, M. Hadad, S. Siegmann, M. Staia, *Surf. Coat. Technol.* **2008**, *202*, 4411.
- [9] M. Arai, *J. Soc. Mater. Sci.* **2009**, *58*, 917.
- [10] M. Adam, M. Rudolphi, D. Koch, *Forschungsvereinigung Verbrennungskraftmaschinen e. V. -DFG/FVV Forschungsvorhaben (FVV Nr. 1108 und 1195)* **2018**.
- [11] S. Primig, H. Leitner, H. Clemens, A. Lorich, W. Knabl, R. Stickler, *Int. J. Refract. Met. Hard Mater.* **2010**, *28*, 703.
- [12] J. Hutchinson, Z. Suo, *Advances in Applied Mechanics*, Elsevier, Amsterdam **1991**, pp. 63–191.
- [13] R. P. Panakarajupally, G. N. Morscher, J. Shi, *J. Eng. Gas Turbines Power* **2023**, *146*, 021008.
- [14] M. D. Thouless, *J. Am. Ceram. Soc.* **1990**, *73*, 2144.
- [15] F. Delannay, P. Warren, *Acta Metall. Mater.* **1991**, *39*, 1061.